Journal of Materials Chemistry A

ROYAL SOCIETY OF CHEMISTRY

COMMUNICATION

View Article Online
View Journal | View Issue

Cite this: J. Mater. Chem. A, 2023, 11, 10155

Received 5th March 2023
Accepted 27th April 2023

DOI: 10.1039/d3ta01343j

rsc.li/materials-a

A polythiourea protective layer for stable lithium metal anodes†

Xiaoya He,‡[a] Zhu Liu,‡[a] Yulian Yang,‡[b] Zhiyong Wang,[a] Yuanmao Chen,[a] Qicheng Zhang,[a] Zhangqin Shi,[a] Yihong Tan,*[a] Xinyang Yue*[a] and Zheng Liang *[a]

Uncontrolled Li dendrite growth and low Coulombic efficiency severely limit the practical applications of Li metal batteries (LMBs). Establishing a stable solid electrolyte interphase (SEI) on the surface of the Li metal anodes (LMAs) is considered to be an effective solution. Here, we report an organic–inorganic composite SEI at the molecular level that effectively reduces the consumption of electrolytes during SEI formation. The artificial SEI layer consists of Li salts and polythiourea. Upon cycling, inorganic components including LiF, Li_2S and Li_3N formed *in situ*, which enhanced the mechanical properties of the composite SEI and guaranteed facile ion transport. In addition, polythiourea itself carries abundant S atoms and polar groups, which can be closely bonded with LMAs to suppress the growth of Li dendrites. The polar groups can also guide a uniform Li^+ flux and form a stable structure over a long period of time. The employment of an organic–inorganic SEI enables high efficiency Li deposition and stable cycling of Ni-rich Li||$LiNi_{0.88}Co_{0.09}Mn_{0.03}O_2$ (NCM88) cells. After 240 cycles, the capacity retention rate is 83.5%. This work provides another artificial SEI design with a promising building block.

[a]*Frontiers Science Center for Transformative Molecules, School of Chemistry and Chemical Engineering, Shanghai Jiao Tong University, Shanghai 200240, P. R. China. E-mail: liangzheng06@sjtu.edu.cn*

[b]*State Key Laboratory of Luminescent Materials and Devices, Center for Aggregation-Induced Emission, South China University of Technology, Guangzhou 510640, China*

† Electronic supplementary information (ESI) available. See DOI: https://doi.org/10.1039/d3ta01343j

‡ These authors contributed equally to this work.

Dr Zheng Liang is an associate professor at the Frontiers Science Center for Transformative Molecules, School of Chemistry and Chemical Engineering, Shanghai Jiao Tong University. He received a bachelor's degree from both the University of Michigan Ann Arbor (2011) and Shanghai Jiao Tong University (2011). Afterwards, he earned a PhD from Stanford University (2018) and continued working as a postdoctoral researcher at Lawrence Berkeley National Laboratory. His research focuses on next-generation Li-ion batteries, Li metal batteries and spent battery recycling.

Introduction

Lithium-ion batteries (LIBs) have been widely used in numerous energy storage applications, such as portable electronics and electric vehicles.[1–3] However, current LIBs are approaching their capacity limits and cannot meet the market demand.[4–7] Therefore, next-generation electrode materials are highly demanded and Li metal is considered as one of the most promising anodes due to its high specific capacity (3860 mA h g^{-1}), low reduction potential (−3.04 V *vs.* SHE) and low weight density (0.53 g cm^{-3}).[8–10] Nevertheless, the inherent dendrite growth and consequent thermal runaway of a Li metal anode (LMA) make LMBs difficult to be commercialized.[11–14] In addition, the LMA and the electrolyte spontaneously form a solid electrolyte interphase (SEI) that is fragile during cycling. This will further consume the active material and electrolyte, resulting in low Coulombic efficiency and capacity degradation.[15–18] Therefore, the LMA needs a more robust SEI.[19]

Over the past few decades, there are two main strategies to enhance an SEI. One is to modify the electrolyte system by changing the electrolyte composition, including solvents, lithium salts and additives, to *in situ* design an SEI with improved stability.[20–24] Another is to construct an artificial SEI with specific components *ex situ*.[25–28] Compared with electrolyte modification, the fabrication of an artificial SEI has certain advantages due to its high controllability, which can passivate the Li metal surface without consuming the limited electrolyte and possess excellent mechanical properties.[29–32] In particular, the research on inorganic and organic composite artificial SEIs has shown good application prospects.[26,33–36] An inorganic layer has high chemical stability in a LMA, but lacks flexibility. Hence

compositing with an organic layer can effectively accommodate the volume fluctuation. Moreover, the use of organic components with self-healing ability will further enhance the lifetime of an artificial SEI.[15,37] These benefits of an inorganic–organic composite SEI layer make it an ideal SEI structure for LMAs.

Thiourea (THU), as an electrolyte additive, has been widely studied.[38–41] Due to the existence of an extended π bond between the C=S double bond and two N atoms in its molecular structure, THU is chemically inert towards LMA. In addition, the high adsorption energy of S atoms to Li can maintain close contact with the Li surface and stabilize the electrode/electrolyte interface. Park's group reported that thiourea as an electrolyte additive could reduce the decomposition of lithium salt and inhibit the growth of lithium dendrites to form a stable SEI layer, thus effectively improving the cycle performance of batteries. Afterwards, Zhou's group proposed a superfilling leveling mechanism using thiourea again as the electrolyte additive, which could promote Li growth on the concave surface of Li metal, thus improving the battery performance at high current densities and high capacities.[38,39] Thiourea directly used as an electrolyte additives is a simpler way and also has some advantages. However, as an organic small molecule additive, the S atoms in thiourea combining with Li metal to prevent contact between the electrode and the electrolyte may not be sufficient; on the other hand, the mechanical strength of the SEI formed spontaneously on the surface of Li metal is low, and it is difficult to avoid a side reaction between electrolyte and Li metal.

Herein, in this work, we synthesized a rigid and flexible polythiourea (PSN) molecule containing benzene ring and carbon chain structures. This was applied to LMBs as an artificial SEI. As shown in Fig. 1b, sulfur atoms in PSN can be adsorbed onto the surface of Li metal, and nitrogen-containing polar groups can effectively regulate the Li ion flux and influence the formation and distribution of lithium deposits, so that lithium can be deposited uniformly,[35,42] whereas in Fig. 1a, for bare Li, due to the uneven distribution of Li ions, a large amount of lithium dendrites and dead lithium formed during the cycling. In addition, PSN carries a large number of hydrogen bonded thiourea units, which have a certain mechanical strength and self-healing ability.[43] The content of inorganic components in PSN films can be increased significantly by the addition of lithium bis(trifluoromethanesulfonyl)imide (LiTFSI). During the cycling process, LiTFSI decomposes into inorganic components (Li_2S, Li_3N and LiF), which enhances Li-ion transport within the SEI and the Young's modulus of the PSN film.[44] The excellent Li-ion transport and mechanical properties are conducive to the formation of a non-dendritic surface and reduce the serious side reaction between LMA and electrolyte. Based on these characteristics, a LMA coated with PSN can prolong the life of symmetrical Li cells at different current densities. The full-cell tests using NCM88 as the cathode showed improved capacity retention and rate performance. The capacity retention of Li||NCM88 cells with PSN is 83.5% after 240 cycles, and its capacity is more than twice that for cells using bare Li at a current density of 0.6 A g^{-1}. It can be seen that our work confirms the effectiveness of a polythiourea coating on the stability of LMAs.

Experimental

Organic–inorganic composite SEI preparation

The synthesis procedure of PSN[45] was summarized in the ESI.† 10 mg PSN and 10 mg LiTFSI were dissolved in 2 mL DMF, and fully stirred at room temperature for 5 h. 500 μm Li foil was soaked in the solution for 30 s, quickly rotated in a spinning machine at high speed, and then dried at 50 °C to obtain the resulting Li foil covered with a uniform film.

Electrochemical measurements

Coin cells (CR2032) were assembled in an Ar-filled glove box with H_2O and O_2 <0.1 ppm. The electrolyte used in this study is 1.0 M $LiPF_6$ in EC–DEC–5%FEC. For each coin cell, 70 μL electrolyte was added. The diameters of Li foil and the NCM88

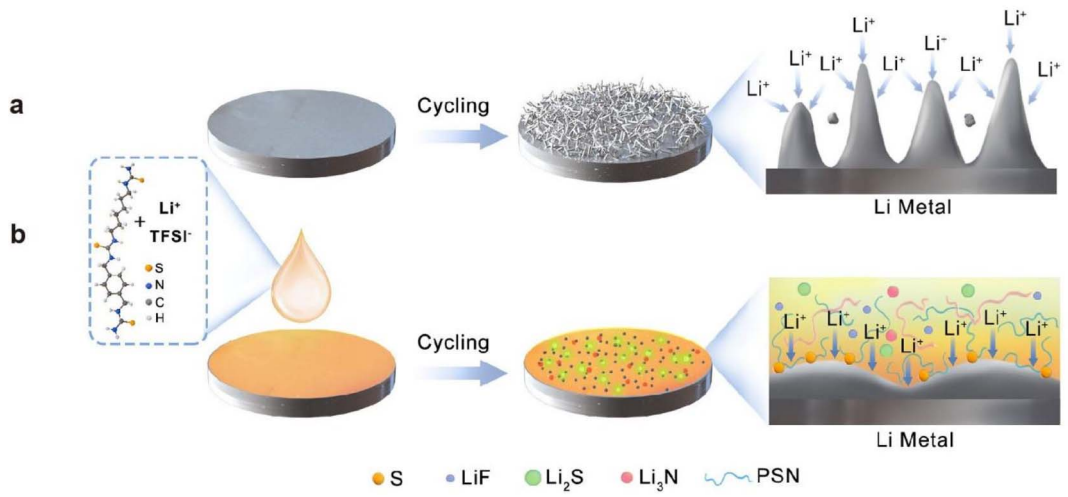

Fig. 1 Schematic illustration of the Li deposition behavior without (a) and with (b) an inorganic–organic artificial SEI protection layer.

cathode electrode are 15.8 mm and 12 mm, respectively, and the specific mass loading of NCM88 is around 10.5 mg cm^{-2}. The Li||NCM88 cells were cycled at 1C rate over the voltage range of 3–4.3 V *vs.* Li/Li^+ at 30 °C. The electrochemical tests were conducted using a Land CT2001A battery test system.

Characterization

A Hitachi 3400N environmental scanning electron microscope was used to obtain top-view and cross-section images after Li plating/stripping. The XPS analytical instrument is from Shimadzu, and the pre- and post-cycling coated lithium was transferred directly from the argon glove box to the XPS system for XPS analysis of Li metal surfaces. Time of flight secondary ion mass spectrometry (TOF-SIMS) uses a Bi source analysis gun (LMIG) as the analysis source, and the model is TOF SIMS 5. The morphology and Young's modulus of Li metal were examined by atomic force microscopy (MFP-3D).

Results and discussion

To construct a stable and robust SEI for a LMA, a polythiourea (PSN) molecule containing a large number of hydrogen bonded thiourea units as well as benzene rings and carbon chains was synthesized by a mild-condition method of multi-component polymerization (MCP) at room temperature.[45] The synthesis procedures are shown in Fig. S1 and S2.† The successful synthesis of PSN was confirmed by their ^1H and ^{13}C nuclear magnetic resonance spectroscopy (NMR) spectra (Fig. 2a and S2†). The characteristic –NH– peaks at δ 7.46/7.73 all emerged in their ^1H NMR spectra, and the characteristic C=S peaks at δ 183.0 emerged in their ^{13}C NMR spectra, confirming the polythiourea structures. The chemical structure of PSN was analyzed by Fourier transform infrared spectroscopy (FTIR). The typical absorption peaks of C=S (1553.4 cm^{-1}) and –NH– (3238.7 cm^{-1}) of PSN (Fig. 2b, green line) and the surface of PSN-coated copper foil (Fig. 2b, orange line) were observed, indicating that the composite film was successfully integrated with the substrate. The typical gel permeation chromatography (GPC) of PSN showed that M_n of the polymer was 7392 g mol^{-1}, as shown in Fig. 2c.

To obtain the optimal composite film, mixed solutions of lithium salts and PSN with different concentrations were prepared, and the Li metal foil was soaked, spin coated and dried to obtain Li-PSN@LiTFSI. The electrochemical impedance spectrum (EIS) of the symmetrical cell was measured to screen out the concentration of the optimal proportion, as shown in Fig. S3a and b.† When the weight percentages of PSN and LiTFSI were both 0.5 wt%, the impedance was minimal. Therefore, the composite film prepared with this concentration was selected for subsequent cell testing and characterization. The morphology of the artificial SEI was characterized by scanning electron microscopy (SEM). The cross-sectional SEM image shows that the LMA exhibits an excellent attachment with the artificial SEI, and the thickness of the artificial SEI is about 100 nm (Fig. 2d). In Fig. 2e, the SEM image of the top view shows that the surface of Li metal coated with an artificial SEI film is smooth except for the trace of spin coating, and there are

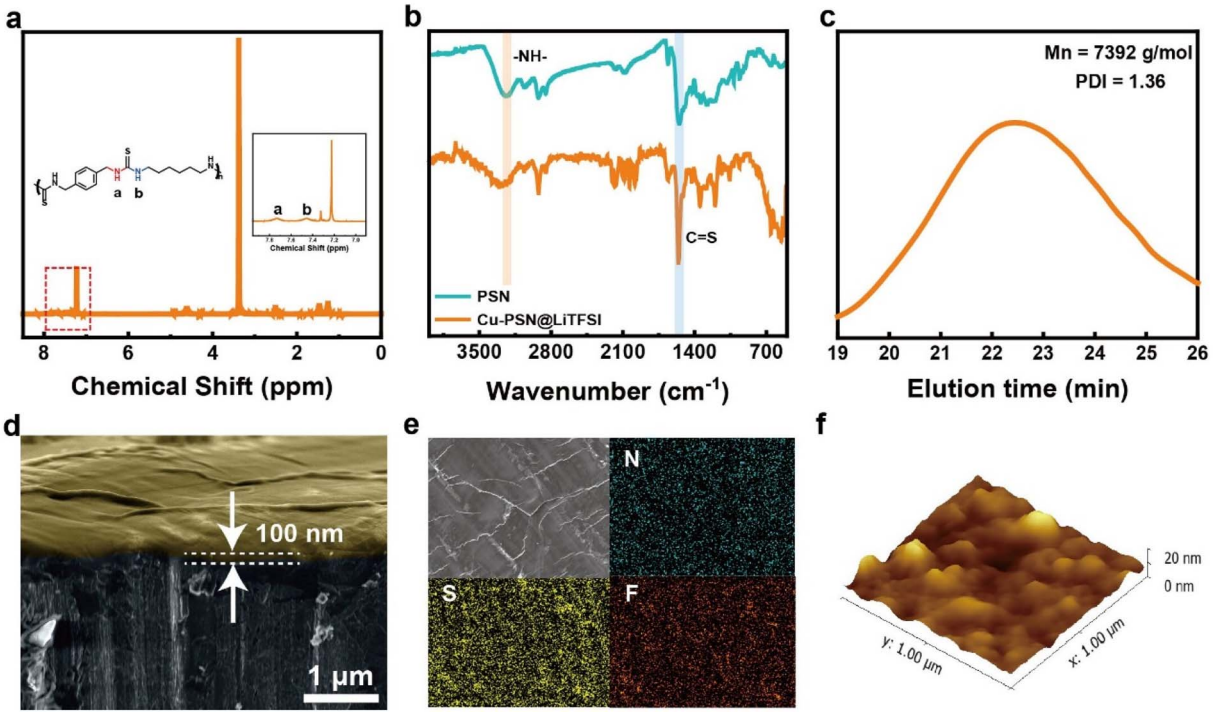

Fig. 2 (a) ^1H NMR spectra of PSN, and the inset is the enlarged feature peak. (b) ATR-FTIR spectra of PSN and Cu-PSN@LiTFSI. (c) GPC spectrum of PSN. The SEM images of the cross section (d) and top view (e) of the coated copper surface (top left corner), and the elemental distributions from EDS of PSN@LiTFSI. (f) AFM image of the Li-PSN@LiTFSI anode.

no holes or cracks between the LMA and the artificial SEI. N, S and F elements are uniformly distributed over the surface. The morphology of the Li-PSN@LiTFSI anode (Fig. 2f) was relatively smooth as measured by using an atomic force microscope (AFM). Due to the continuous protection of the artificial SEI, it is favorable for long-term stable cycling.

In order to prove that an inorganic–organic artificial SEI can effectively regulate Li deposition morphology and the role of PSN@LiTFSI in Li deposition, we deposited Li on Cu with a capacity of 3.0 mA h cm^{-2} and a current density of 0.5 mA cm^{-2}. The morphology was characterized by SEM. From the top-view and cross-sectional SEM images, it was observed that the surface of the bare Li after depositing is uneven and has loose lithium dendrites (Fig. 3a and b). In marked contrast, the surface of Li metal coated with PSN@LiTFSI is very dense and smooth, which can also be seen from the cross section (Fig. 3c and d). Lithium deposition behavior was further investigated by *in situ* optics. At a current density of 0.4 mA cm^{-2}, it was deposited for 0, 40, and 80 min, respectively (Fig. S4†). With the increase of deposition time, Li-PSN@LiTFSI can maintain a dense dendrite-free Li morphology, while fluffy Li layers with long dendrites were observed on the bare Li surface. In addition, the contact angle test shows that the contraction angle of Li-PSN@LiTFSI is much smaller than that of bare Li, indicating that it has ultra-good electrolyte wettability, contributing to fast Li-ion transport and uniform Li-ion flux (Fig. S5†). Atomic force microscopy (AFM) was used to measure the Young's modulus of the Li-PSN@LiTFSI surface before and after the cycle. The average Young's modulus of the artificial coating after cycling is 3 GPa (Fig. 3f), which is higher than 2 GPa before the cycle (Fig. 3e), indicating that the inorganic salts generated *in situ* during cycling can enhance the Young's modulus of the composite film and help to inhibit the growth of lithium dendrites.

To investigate the effect of an inorganic–organic artificial SEI on the long-term stability of the LMA, Coulombic efficiency (CE) of Li plating/stripping was evaluated using an Li||Cu cell at a current density of 0.5 mA cm^{-2}; the amount of Li deposition is 0.5 mA h cm^{-2}. It is observed that the half cell with an inorganic–organic artificial SEI can stably cycle in the carbonate solvent for 120 cycles with a higher CE of 95.7% (Fig. 4a), while bare Cu exhibits only 40 cycles with a lower CE of 93.7%. When the Li deposition amount is 1 mA h cm^{-2}, the inorganic–organic artificial SEI exhibits a CE of 97.6% after 120 cycles. In comparison, the CE of the reference sample is approximately 96.5% after 80 cycles (Fig. S6†). In addition, the voltage polarization profiles of Li plating/stripping at 0.5 mA cm^{-2}/0.5 mA h cm^{-2} indicates that the half cell with a PSN protective coating has lower polarization and higher stability (Fig. 4b and S7†). The Li||Li symmetric cell test was also used to compare the stability of LMA cycling in bare Li and Li-PSN@LiTFSI at different current densities of 1 and 3 mA cm^{-2}. As shown in Fig. S8,† the symmetrical cells showed substantial voltage fluctuation after only about 300 h in bare Li at a current density of 1.0 mA cm^{-2}, which could be explained by the dendrite formation after repeated lithium plating and stripping. However, the symmetrical cells with a coated protective layer demonstrate a flat voltage plateau over 800 hours, which is greatly superior to bare Li. Moreover, when the current density was increased to 3.0 mA cm^{-2} (Fig. 4c), the gradually increasing voltage hysteresis was observed for the symmetrical cells with bare Li, which was attributed to the thickening of the SEI film

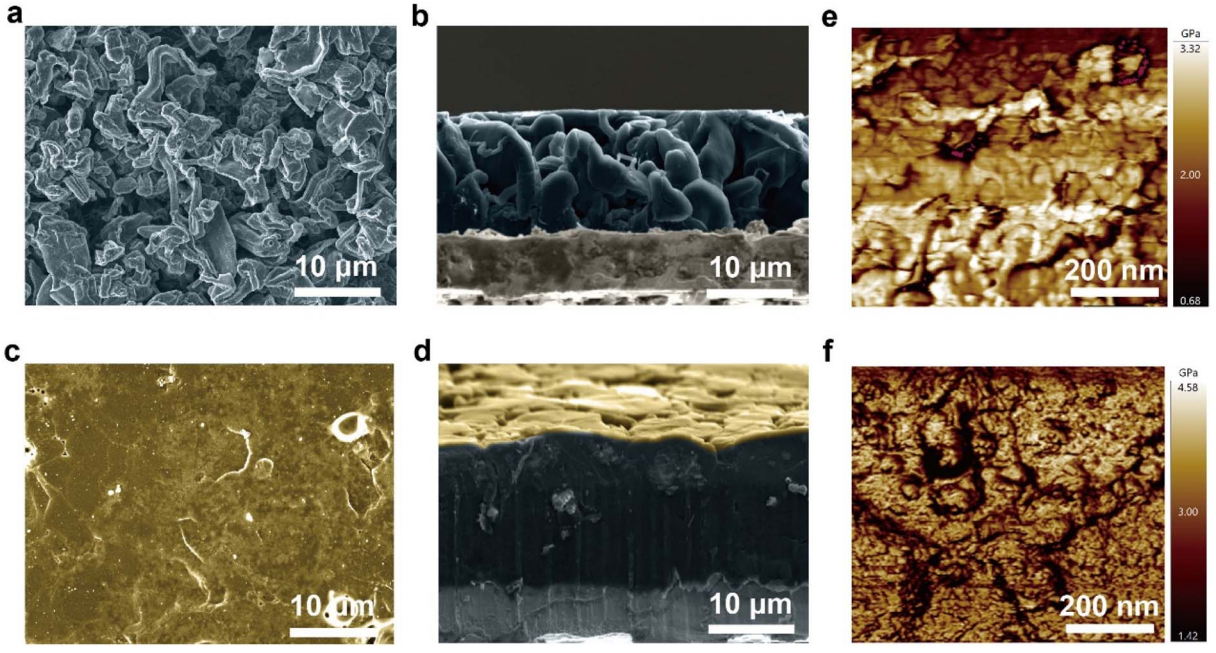

Fig. 3 (a) Top-view SEM image and (b) cross-sectional SEM image of Li metal deposited on Cu with a capacity of 3.0 mA h cm^{-2}. (c) and (d) are the top-view SEM image and side-view SEM image of Li metal deposited on a Cu-PSN@LiTFSI substrate with a capacity of 3.0 mA h cm^{-2}, respectively. Young's modulus mapping from AFM of Li-PSN@LiTFSI before cycling (e) and after cycling (f).

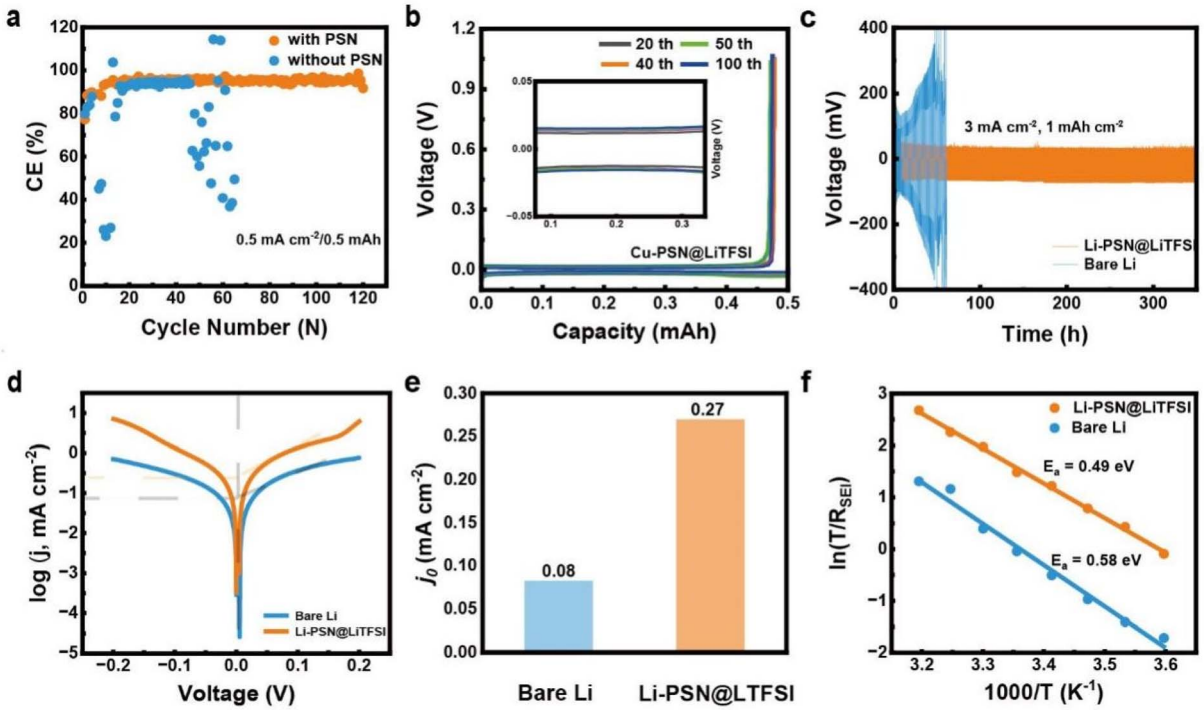

Fig. 4 (a) CEs of Li||Cu cells with or without PSN@LiTFSI coating. (b) Voltage polarization profiles of Li||Cu cells at 0.5 mA cm^{-2} with a capacity of 0.5 mA h cm^{-2} in the 20th, 40th, 50th and 100th cycle. (c) Symmetric cells at 3 mA cm^{-2}/1 mA h cm^{-2} using Li-PSN@LiTFSI and bare Li electrodes. (d) Tafel plots of symmetric cells and (e) the calculated exchange current densities (j_0). (f) Arrhenius plots of the reciprocal R_{SEI} and the calculated activation energy for Li^+ diffusion through a SEI.

and the generation of dead Li during the plating/stripping process. In contrast, symmetrical cells with a PSN@LiTFSI protective layer of Li still show a very smooth cycle after 350 h. Similar results were obtained when using PSN@LiTFSI-protected thin Li (50 μm) (Fig. S9†). Electrochemical studies on the plating/stripping kinetics of lithium and charge transfer in the SEI were carried out by using a symmetrical cell. The exchange current density was adopted here to demonstrate the charge transfer kinetics of the artificial SEI. The Tafel plots (Fig. 4d) obtained from the intercept and the corresponding exchange current density (j_0, Fig. 4e) demonstrated that the j_0 of Li-PSN@LiTFSI (0.27 mA cm^{-2}) is higher than that of bare Li (0.08 mA cm^{-2}). It indicates that its charge transfer ability is superior to that of a self-forming SEI, which also reflects its better interaction with deposited Li metal and is conducive to more uniform Li deposition. Furthermore, the activation energy for Li deposition was calculated from the variable-temperature-controlled R_{SEI} values. By linearly fitting ln(1/R) *versus* 1/T, as shown in Fig. 4f, the apparent activation energies obtained from the slopes are determined to be 0.49 and 0.58 eV for Li-PSN@LiTFSI and bare Li, respectively. These results indicated that the Li-PSN@LiTFSI anode is conducive to the rapid diffusion of Li ions.

To further understand the changes of the chemical composition of the anode surface after 20 cycles, Li-PSN@LiTFSI was collected for X-ray photoelectron spectroscopy (XPS) analysis after cycling. As shown in Fig. 5a, the peak of 688.6 eV in the F 1s spectrum before cycling can be attributed to LiTFSI. The concentration of LiTFSI was significantly reduced after cycling while the peak of LiF appeared at 684.6 eV, which means that a considerable part of the LiTFSI was decomposed to LiF *in situ* after cycling. In the N 1s spectrum, there were LiTFSI peaks at 399.5 eV before and after cycling, and the content decreased after cycling. This also indicates that LiTFSI is partially decomposed during cycling, which could be explained by the F 1s and S 2p spectra (Fig. 5b). After cycling, the peak of PSN could also be observed at 400.5 eV, and the decomposition product Li_3N appears at 397.0 eV, which was consistent with the results of TOF-SIMS. In the S 2p spectrum, the peaks at 161.83 eV and 162.63 eV could be attributed to polythiourea (Fig. S10†), while the LiTFSI peak at 168.9 eV and the Li_2SO_4 peak at 169.7 eV could be attributed to the introduction of LiTFSI (Fig. 5c). After cycling, the peaks of LiTFSI and PSN could still be observed, confirming that the composite artificial SEI film still remained on the surface of Li metal. In addition, there were additional Li–S peaks at 160.0 eV, which could be attributed to Li–S bonding of Li_2S.[46] This result for the S 2p spectrum was consistent with that for TOF-SIMS below. The XPS results clearly showed that the artificial SEI composite film still existed stably after cycling and the surface was accompanied by the *in situ* formed inorganic Li salts including Li_2S, LiF, and Li_3N from LiTFSI decomposition.

To further study the change and stability of the artificial SEI composite film after cycling, the symmetrical cell was measured by TOF-SIMS before and after 20 cycles. The normalized to maximum depth profile of various species of interest is shown

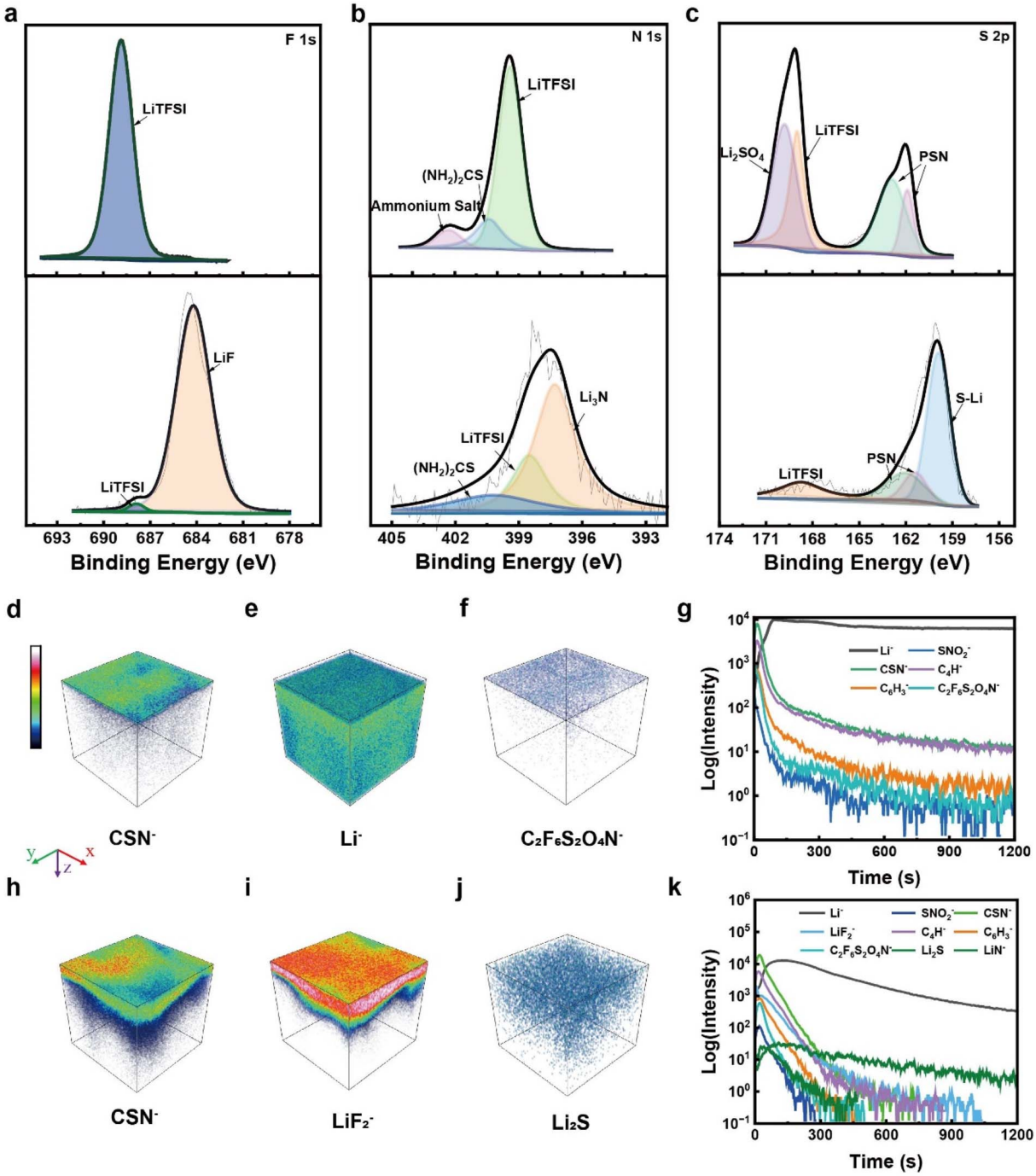

Fig. 5 XPS spectra of the Li-PSN@LiTFSI surface before (upper part of a–c) and after 20 cycles (lower part of a–c). TOF-SIMS shows the spatial distribution of the species that constitute the artificial SEI on the Li metal surface before and after the cycling. (d–f) show three-dimensional (3D) views of the depth profile before cycling, and (h–j) show the depth profile of Li-PSN@LiTFSI after cycling. (g and k) Determination of the chemical composition and depth location of the SEI layer before (g) and after cycling (k).

according to the depth analysis curve of the Li metal anode in negative ion mode. The depth profile curve of Li-PSN@LiTFSI before cycling is shown in Fig. 5g. The fragment peaks CSN^-, $C_6H_3^-$, and C_4H^- of PSN can be observed, as well as the fragment peaks $TFSI^-$ and SNO_2^- ascribed to lithium salt. 3D views of these sections are depicted in Fig. 5d–f, showing the structure of the composite artificial SEI film. The signal of the fragment peak of PSN was still strong after cycling, indicating that the composite film remained stable on the surface of Li metal after the plating/stripping process (Fig. 5k). In addition, new species such as LiF^-, Li_2S and LiN^- were found to be distributed over the entire composite film, mainly from the decomposition of LiTFSI dispersed in the PSN membrane, which was consistent with the results of XPS. This is also reflected in 3D

reconstructions of the TOF-SIMS data for CSN^-, LiF^-, Li_2S, LiN^- and $C_2F_6S_2O_4N^-$ secondary ions, showing the distribution of these species throughout the sputtering depth (Fig. 5h–j and S11†). The formation of inorganic LiF, Li_2S and Li_3N is helpful to improve the mechanical strength and ionic conductivity of the artificial SEI composite film. This is also consistent with the results of the AFM tests. Meanwhile, the improvement of PSN@LiTFSI for ionic conductivity of an LMA can also be indirectly explained by comparing the EIS tests after cycling. In particular, after cycling, the artificial SEI exhibits a much lower interfacial resistance than bare Li (Fig. S12†). In order to further prove the stability of PSN, the characteristic peaks of PSN, –NH– (3238.7 cm^{-1}) and C=S (1553.4 cm^{-1}) were observed in the infrared spectra of the copper coated surface after cycling (Fig. S13†). Similarly, the morphology and the uniform distribution of C, N, S and F elements in energy dispersion X-ray spectra (EDS) after 20 (Fig. S14†) and 100 cycles (Fig. S15†) also confirmed the stable existence of the composite films.

The performance of Li-PSN@LiTFSI in a LMB was further investigated by coupling with an NCM88 cathode. As shown in Fig. 6a, the Li-PSN@LiTFSI||NCM88 cell could stably cycle for more than 240 cycles with a capacity retention rate of 83.5% at a current density of 1C. When using PSN@LiTFSI-protected thin Li (50 μm), it can be cycled for 260 cycles with a capacity retention rate of 80% (Fig. S16†). In contrast, the capacity of Li||NCM88 cells gradually decreased, and the capacity retention rate was 76% after 200 cycles. It is shown that PSN@LiTFSI plays a crucial role in stabilizing the LMA. In addition, we also tested the full cell with a thick protective film of about 200 nm. Due to the high impedance, the capacity attenuated to 80% after only 180 cycles (Fig. S17a–c†). The charge/discharge voltage profiles indicated lower polarization of Li-PSN@LiTFSI as compared to that of bare Li (Fig. 6c and S18a–c†). The NCM88 cells were also cycled at different rates to study the effect of current density on the Li anodes. More importantly, Li-PSN@LiTFS has good capacity retention even at high charge/discharge rates (Fig. 6b). And the degree of overvoltage is lower than that of bare Li

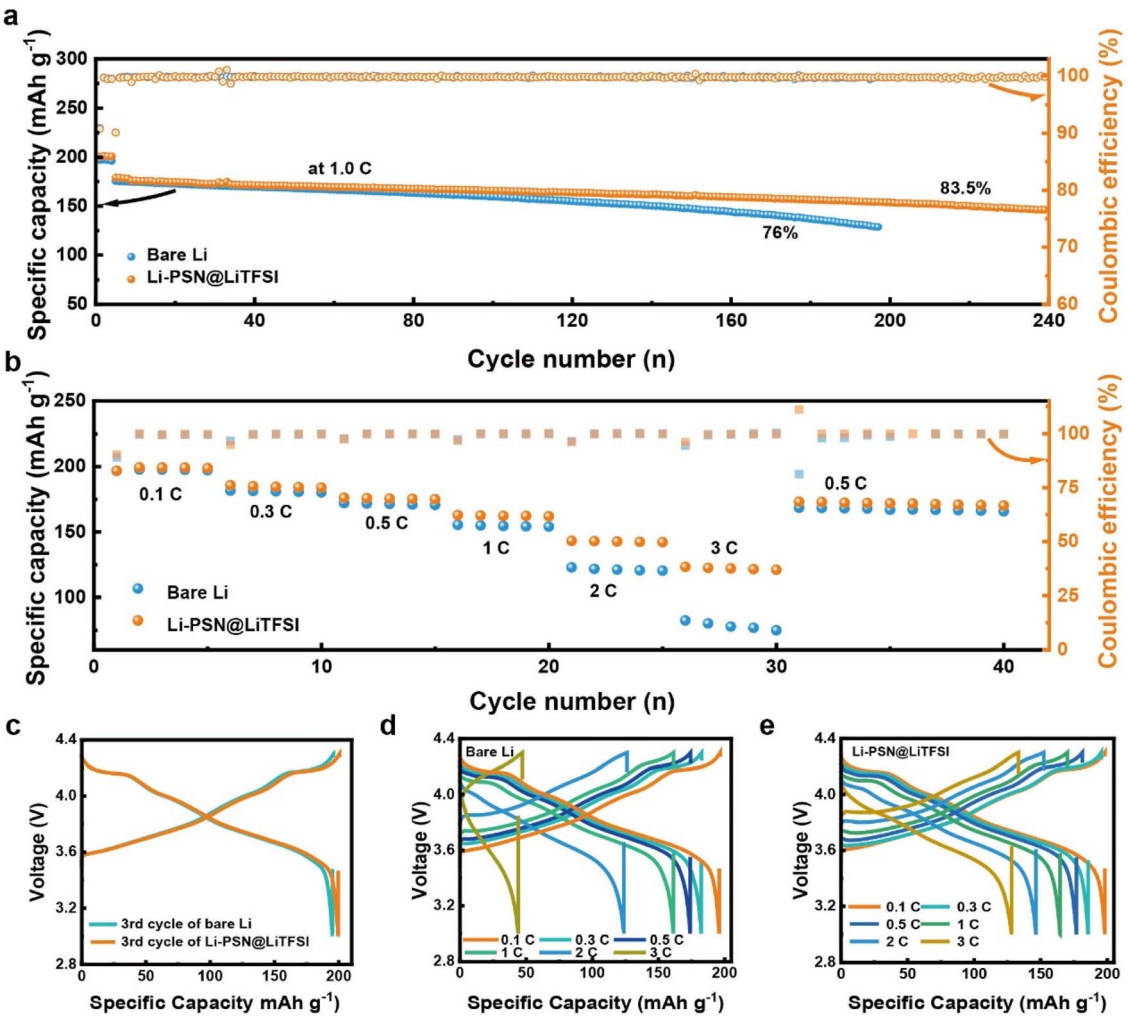

Fig. 6 Electrochemical performance of a Li||NCM88 cell. (a) Discharge capacity and Coulombic efficiency of Li-PSN@LiTFSI||NCM88, bare Li||NCM88 performance at 1C. and (b) rate capability of full cells with Li-PSN@LiTFSI and bare Li for cycling from 0.1 to 3C. (c) Voltage profiles of bare Li and Li-PSN@LiTFSI in the third circle. (d and e) Charge/discharge voltage profiles of NCM88 full cells with (d) bare Li and (e) Li-PSN@LiTFSI at various current densities.

(Fig. 6d, e and S19a–c†). The improved full cell performance indicated that the polar groups in a polythiourea film could even out the distribution of Li ions during plating/stripping and promote fast ion transport kinetics.

Conclusion

In summary, a novel organic–inorganic composite SEI using polythiourea was prepared on the LMA, generating inorganic Li_3N, Li_2S and LiF *in situ*. The lithium deposition was controlled by improving the mechanical strength and ionic conductivity of the composite film as well as homogenizing the Li ion flux, showing uniform lithium deposition and stable electroplating/stripping performance. Based on the above characteristics, a symmetrical cell with a PSN composite film can stably cycle for more than 800 h (1 mA cm^{-2}, 1 mA h cm^{-2}). When the current density increases to 3 mA cm^{-2}, the lifetime of Li-PSN@LiTFSI is significantly extended about five times than in cells using bare Li. In Li||NCM88 full cells, Li-PSN@LiTFSI cells performed a stable cycling with a capacity retention of 83.5% after 240 cycles. At a high rate of 3C, its capacity is much higher than that of bare Li. A comprehensive study and deep understanding of the anode surface using AFM, XPS and TOF-SIMS show the positive role of the composite film. This study provides a new promising candidate for an artificial SEI towards a stable and safe Li metal anode.

Author contributions

X. H., Z. L. and Y. Y. contributed equally to this work. X. H.: investigation, visualization, and writing; Z. L.: supervision and validation; L. Y.: investigation, synthesis and characterization; Z. W.: investigation. Y. C.: methodology; Q. Z.: data curation; Z. S.: investigation; Y. T.: investigation; X. Y.: methodology; Zheng Liang: conceptualization, methodology, supervision, and funding acquisition.

Conflicts of interest

There are no conflicts to declare.

Acknowledgements

This work was supported by the National Natural Science Foundation of China (NSFC) under Grant No. 52102282, the Young Elite Scientists Sponsorship Program by CAST (2020QNRC001), and start-up funds from Shanghai Jiao Tong University.

References

1 D. Deng, *Energy Sci. Eng.*, 2015, **3**, 385–418.
2 B. Diouf and R. Pode, *Renewable Energy*, 2015, **76**, 375–380.
3 A. Opitz, P. Badami, L. Shen, K. Vignarooban and A. M. Kannan, *Renewable Sustainable Energy Rev.*, 2017, **68**, 685–692.
4 L. Fan, H. L. Zhuang, L. Gao, Y. Lu and L. A. Archer, *J. Mater. Chem. A*, 2017, **5**, 3483–3492.
5 Y. Lu, Z. Tu and L. A. Archer, *Nat. Mater.*, 2014, **13**, 961–969.
6 J. P. Pender, G. Jha, D. H. Youn, J. M. Ziegler, I. Andoni, E. J. Choi, A. Heller, B. S. Dunn, P. S. Weiss, R. M. Penner and C. B. Mullins, *ACS Nano*, 2020, **14**, 1243–1295.
7 J. F. Peters, M. Baumann, B. Zimmermann, J. Braun and M. Weil, *Renewable Sustainable Energy Rev.*, 2017, **67**, 491–506.
8 X. Shen, H. Liu, X.-B. Cheng, C. Yan and J.-Q. Huang, *Energy Storage Mater.*, 2018, **12**, 161–175.
9 Q. Wang, H. Wang, J. Wu, M. Zhou, W. Liu and H. Zhou, *Nano Energy*, 2021, **80**, 105516–105552.
10 R. Wang, W. Cui, F. Chu and F. Wu, *J. Energy Chem.*, 2020, **48**, 145–159.
11 G. Bieker, M. Winter and P. Bieker, *Phys. Chem. Chem. Phys.*, 2015, **17**, 8670–8679.
12 X. Zhang, A. Wang, X. Liu and J. Luo, *Acc. Chem. Res.*, 2019, **52**, 3223–3232.
13 T. Li, X.-Q. Zhang, P. Shi and Q. Zhang, *Joule*, 2019, **3**, 2647–2661.
14 D. Wang, W. Zhang, W. Zheng, X. Cui, T. Rojo and Q. Zhang, *Adv. Sci.*, 2017, **4**, 1600168–1600179.
15 K. Liu, A. Pei, H. R. Lee, B. Kong, N. Liu, D. Lin, Y. Liu, C. Liu, P. C. Hsu, Z. Bao and Y. Cui, *J. Am. Chem. Soc.*, 2017, **139**, 4815–4820.
16 X. B. Cheng, R. Zhang, C. Z. Zhao, F. Wei, J. G. Zhang and Q. Zhang, *Adv. Sci.*, 2016, **3**, 1500213–1500233.
17 Y. Wang, E. Sahadeo, G. Rubloff, C.-F. Lin and S. B. Lee, *J. Mater. Sci.*, 2018, **54**, 3671–3693.
18 F. Wu, Y.-X. Yuan, X.-B. Cheng, Y. Bai, Y. Li, C. Wu and Q. Zhang, *Energy Storage Mater.*, 2018, **15**, 148–170.
19 J. Zeng, Q. Liu, D. Jia, R. Liu, S. Liu, B. Zheng, Y. Zhu, R. Fu and D. Wu, *Energy Storage Mater.*, 2021, **41**, 697–702.
20 E. Markevich, G. Salitra, F. Chesneau, M. Schmidt and D. Aurbach, *ACS Energy Lett.*, 2017, **2**, 1321–1326.
21 J. Qian, W. Xu, P. Bhattacharya, M. Engelhard, W. A. Henderson, Y. Zhang and J.-G. Zhang, *Nano Energy*, 2015, **15**, 135–144.
22 J. Zheng, M. H. Engelhard, D. Mei, S. Jiao, B. J. Polzin, J.-G. Zhang and W. Xu, *Nat. Energy*, 2017, **2**, 17012–17020.
23 L. Suo, Y. S. Hu, H. Li, M. Armand and L. Chen, *Nat. Commun.*, 2013, **4**, 1481–1490.
24 Q. Wu, Y. Qian, X. Tang, J. Teng, H. Ding, H. Zhao and J. Li, *ACS Appl. Energy Mater.*, 2022, **5**, 5742–5749.
25 N. W. Li, Y. X. Yin, C. P. Yang and Y. G. Guo, *Adv. Mater.*, 2016, **28**, 1853–1858.
26 G. Zheng, S. W. Lee, Z. Liang, H. W. Lee, K. Yan, H. Yao, H. Wang, W. Li, S. Chu and Y. Cui, *Nat. Nanotechnol.*, 2014, **9**, 618–623.
27 X. Liang, Q. Pang, I. R. Kochetkov, M. S. Sempere, H. Huang, X. Sun and L. F. Nazar, *Nat. Energy*, 2017, **2**, 17119–17126.
28 J. Zhao, M. Hong, Z. Ju, X. Yan, Y. Gai and Z. Liang, *Angew. Chem., Int. Ed.*, 2022, **61**, e202214386–e202214396.
29 J. Wang, J. Yang, Q. Xiao, J. Zhang, T. Li, L. Jia, Z. Wang, S. Cheng, L. Li, M. Liu, H. Liu, H. Lin and Y. Zhang, *Adv. Funct. Mater.*, 2020, **31**, 2007434–2007444.

30 Y. Zhao, G. Li, Y. Gao, D. Wang, Q. Huang and D. Wang, *ACS Energy Lett.*, 2019, **4**, 1271–1278.
31 X.-B. Cheng, C. Yan, H.-J. Peng, J.-Q. Huang, S.-T. Yang and Q. Zhang, *Energy Storage Mater.*, 2018, **10**, 199–205.
32 J.-S. Lee, K. Shin, S.-Y. Jun, S. Kim and W.-H. Ryu, *Chem. Eng. J.*, 2023, **458**, 141383–141394.
33 M. Baloch, D. Shanmukaraj, O. Bondarchuk, E. Bekaert, T. Rojo and M. Armand, *Energy Storage Mater.*, 2017, **9**, 141–149.
34 C. Yang, K. Fu, Y. Zhang, E. Hitz and L. Hu, *Adv. Mater.*, 2017, **29**, 1701169–1701197.
35 J. Yang, C. Hu, Y. Jia, Y. Pang, L. Wang, W. Liu and X. Sun, *ACS Appl. Mater. Interfaces*, 2019, **11**, 8717–8724.
36 J. H. Kim, H. S. Woo, W. K. Kim, K. H. Ryu and D. W. Kim, *ACS Appl. Mater. Interfaces*, 2016, **8**, 32300–32306.
37 P. Chen, L. Li, C. Wang, H. Yi, Q. Wu, L. Song, X. Wu and L. Tan, *Appl. Surf. Sci.*, 2022, **604**, 154468–154474.
38 Q. Wang, C. Yang, J. Yang, K. Wu, C. Hu, J. Lu, W. Liu, X. Sun, J. Qiu and H. Zhou, *Adv. Mater.*, 2019, **31**, 1903248–1903258.
39 V.-C. Ho, D. T. Ngo, H. T. T. Le, R. Verma, H.-S. Kim, C.-N. Park and C.-J. Park, *Electrochim. Acta*, 2018, **279**, 213–223.
40 X. Wu, Y. Li, C. Li, Z. He, Y. Xiang, L. Xiong, D. Chen, Y. Yu, K. Sun, Z. He and P. Chen, *J. Power Sources*, 2015, **300**, 453–459.
41 A. Rafie, R. Pai and V. Kalra, *J. Mater. Chem. A*, 2021, **9**, 26976–26988.
42 T.-T. Su, J.-B. Le, W.-F. Ren, S.-J. Zhang, J.-M. Yuan, K. Wang, C.-Y. Shao, J.-T. Li, S.-G. Sun and R.-C. Sun, *J. Power Sources*, 2022, **521**, 230949–230959.
43 Y. Yanagisawa, Y. Nan, K. Okuro and T. Aida, *Science*, 2018, **359**, 72–76.
44 H. Yuan, J. Nai, Y. Fang, G. Lu, X. Tao and X. W. D. Lou, *Angew. Chem., Int. Ed.*, 2020, **59**, 15839–15843.
45 T. Tian, R. Hu and B. Z. Tang, *J. Am. Chem. Soc.*, 2018, **140**, 6156–6163.
46 Y. Fu, C. Zu and A. Manthiram, *J. Am. Chem. Soc.*, 2013, **135**, 18044–18047.